2001-03

Variable-retardance, Fourier-transform imaging spectropolarimeters for visible spectrum remote sensing

Tyo, J. Scott

Variable-retardance, Fourier-transform imaging spectropolarimeters for visible spectrum remote sensing

J. Scott Tyo and Theodore S. Turner, Jr.

An imaging, variable-retardance, Fourier-transform spectropolarimeter is presented that is capable of creating spectropolarimetric images of scenes with independent characterization of spatial, spectral, and polarimetric information. The device has a spectral resolution of $\sim 225\ \mathrm{cm}^{-1}$, making it truly hyperspectral in nature. Images of canonical targets such as spheres and cylinders obtained in a laboratory setup are presented. The results demonstrate the capability of developing systems to collect spectropolarimetric data of field images by use of the concept of pushbroom scanning and serial collection of polarimetric information. Further development of a parallelized collection strategy would allow the collection of near-real-time images of real-world targets.

OCIS codes: 280.0280, 260.5430, 230.5440.

1. Introduction

Spectropolarimetry has been explored as a method of improving target detection capabilities in various remote sensing applications. In addition to the information available by spectral sensing techniques alone, polarization has the potential to improve target contrast,[1] reduce clutter,[1] aid in the defeat of intervening scatterers,[2,3] and provide orientation information about various target features.[4] In this paper we use a variable-retardance, Fourier-transform spectropolarimeter (VRFTSP) as an integrated device to collect fully seven-dimensional (two spatial, four polarimetric, and one spectral) spectropolarimetric images of canonical targets in a laboratory setup. In Section 2 we describe the instrument design concept. We present a summary of the basic method of analysis of the polarization data in Section 3, and we discuss the details of processing the spectropolarimetric image data in Section 4. In Section 5 we describe the instrument performance as demonstrated by the experimental results. Finally, in Section 6 we provide conclusions and indications of the direction of the planned future research.

2. Instrument Design

A schematic layout of the VRFTSP is shown in Fig. 1. The interferometer (I) is the heart of an existing spatially modulated Fourier-transform instrument[5–7] based on a variation of the Sagnac interferometer by Barnes[8] who added a third mirror converting it from a lateral shear to an angular shear device. Differences in properties between the two configurations, particularly the alignment sensitivities, are discussed in Ref. 5. Rather than the separate optical components used by Barnes, the interferometer is built in nearly monolithic form consisting of two cemented rhombs with a beam-splitter coating in between. Mirror (M1) is mounted separately to allow the tilting that introduces the angular shear producing white-light fringes localized at the mirror. The fringes are reimaged at the camera focal plane array (FPA) by a positive achromat (L1) and a negative cylinder lens (L2) as a set of spatiospectral line images with the spectral or fringe dimension in the plane of the figure and the spatial imaging dimension orthogonal. The spectral dimension can be considered a one-dimensional pupil because the chief rays of the two interfering beams are brought to focus there. For this reason it is desirable to locate the system stop (or its image) at the tilt mirror (M1). The camera is an interline transfer CCD with 768×494 pixels. A frame grabber captures 640×480 images that are computer processed.

The polarimetric components ahead of the inter-

When this research was performed, the authors were with the U.S. Air Force Research Laboratory, Space Vehicles Directorate, Kirtland Air Force Base, New Mexico 87117. J. S. Tyo (tyo@ieee.org) is now with the Department of Electrical and Computer Engineering, Naval Postgraduate School, 589 Dyer Road, Monterey, California 93943-5000. T. S. Turner, Jr., is now with Ball Aerospace Technologies, 2021 Girard Boulevard, SE, Albuquerque, New Mexico 87106.

Received 27 April 2000; revised manuscript received 6 November 2000.

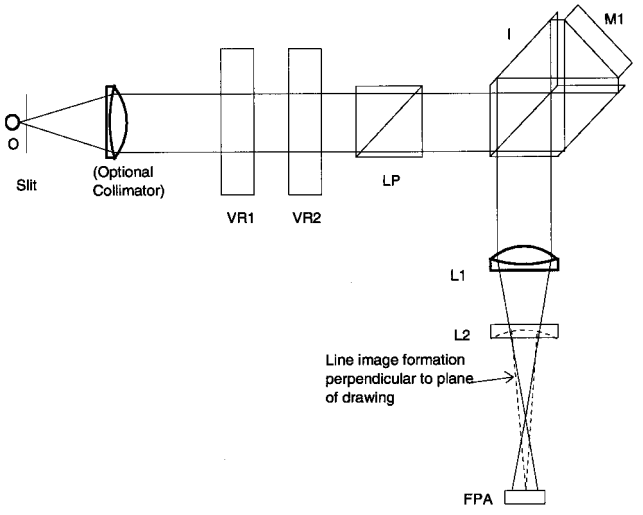

Fig. 1. Schematic of the optical setup of the VRFTSP. The polarimeter (VR1, VR2, LP) is placed in front of the spectrometer (I, L1, L2). The plane of the page represents the interferogram dimension. The cylinder lens (L2) forms an image in the direction perpendicular to the page.

ferometer consist of two voltage-controlled variable liquid-crystal retarders (Meadowlark Optics) (VR1) and (VR2) followed by a linear polarizer (LP) oriented to pass horizontally polarized light. We performed the initial calibration of the retarders at 632.8 nm by determining the voltages for 0° and 180° phase retardance. The procedure was carried out with the retarder mounted between crossed polarizers with its fast axis at 45° with respect to each polarizer. The voltages for 90° retardance were then determined at the half-power intensity of the transmitted light. At other wavelengths the retardance was assumed to vary as $(\pi/2)\lambda_0/\lambda$, where $\lambda_0 = 632.8$ nm. This ignores the dispersion of the liquid-crystal medium which was unknown but assumed to be small, as was borne out subsequently by the experimental results. After calibration VR1 and VR2 were mounted with their fast axes oriented at 45° and 22.5°, respectively, relative to the orientation of the linear polarizer LP.

The optical setup depicted in Fig. 1 uses one spatial dimension of the FPA to obtain spectral information, then uses the temporal dimension to obtain polarization information and the second spatial dimension. This scheme combines the common strategies that are used to build imaging polarimeters and imaging spectrometers separately. An additional alternative would be to use interchangeable filters or a variable filter so that both spatial dimensions are obtained simultaneously. This strategy is common in multispectral systems, but is not used in hyperspectral systems such as the airborne visible infrared imaging spectrometer (AVIRIS)[9] and hyperspectral digital imagery collection experiment (HYDICE).[10] Most hyperspectral systems use the inherent motion of the platform to scan spatially in one dimension of a pushbroom[10] or whiskbroom[9] strategy.

Various objects were mounted on a horizontal translation stage located at position O in Fig. 1. A fixed narrow vertical slit approximately 20 mm in length was placed on the optical axis directly behind the object. At each slit location, a spatiospectral image was formed that consisted of an interferogram along the horizontal dimension of the CCD and a line image along the vertical. We developed the horizontal spatial dimension of the object by scanning the object in a series of steps, which is effectively equivalent to the pushbroom mode of image formation often used in aircraft or satellite operation. For field-deployable units, we propose use of either a moving platform or a scanning mirror to affect the pushbroom mode of operation.

3. Spectropolarimetric Measurements

The transmitted light passing through the polarimeter (VR1, VR2, LP) analyzer in Fig. 1 can be characterized by use of Mueller calculus.[11] The emergent light is represented by the Stokes vector

$$\mathbf{S}_{\text{out}} = (s_{0,\text{out}}\, s_{1,\text{out}}\, s_{2,\text{out}}\, s_{3,\text{out}})^T = \mathbf{M}_{\text{LP}} \cdot \mathbf{M}_{\text{VR2}} \cdot \mathbf{M}_{\text{VR1}} \cdot \mathbf{S}_i, \tag{1}$$

where

$$\mathbf{S}_i = (s_0\, s_1\, s_2\, s_3)^T \tag{2}$$

is the unknown input Stokes vector. The parameter s_0 is the unpolarized intensity, s_1 is the horizontal linearly polarized intensity minus the vertical linearly polarized intensity, s_2 is the 45° linearly polarized intensity minus the 135° linearly polarized intensity, and s_3 is the difference between left- and right-circularly polarized intensities. The quantities $\mathbf{M}_{\text{LP}}$, $\mathbf{M}_{\text{VR1}}$, and $\mathbf{M}_{\text{VR2}}$ are the Mueller matrices representing the linear polarizer and two linear retarders, respectively. These are given for the specific orientations above by

$$\mathbf{M}_{\text{LP}} = \frac{1}{2}\begin{bmatrix} q+r & q-r & 0 & 0 \\ q-r & q+r & 0 & 0 \\ 0 & 0 & 2\sqrt{qr} & 0 \\ 0 & 0 & 0 & 2\sqrt{qr} \end{bmatrix}, \tag{3}$$

$$\mathbf{M}_{\text{VR1}}(\Delta) = \begin{bmatrix} 1 & 0 & 0 & 0 \\ 0 & \cos(\Delta) & 0 & -\sin(\Delta) \\ 0 & 0 & 1 & 0 \\ 0 & \sin(\Delta) & 0 & \cos(\Delta) \end{bmatrix}, \tag{4}$$

$$\mathbf{M}_{\text{VR2}}(\delta) = \begin{bmatrix} 1 & 0 & 0 & 0 \\ 0 & \frac{1}{2}[1+\cos(\delta)] & \frac{1}{2}[1-\cos(\delta)] & -\frac{1}{\sqrt{2}}\sin(\delta) \\ 0 & \frac{1}{2}[1-\cos(\delta)] & \frac{1}{2}[1+\cos(\delta)] & \frac{1}{\sqrt{2}}\sin(\delta) \\ 0 & \frac{1}{\sqrt{2}}\sin(\delta) & -\frac{1}{\sqrt{2}}\sin(\delta) & \cos(\delta) \end{bmatrix}, \tag{5}$$

where q and r are the diattenuation coefficients for the linear polarizer ($q = 1$, $r = 0$ for an ideal polarizer) and Δ and δ are the two phase retardances. Because the detector responds to intensity (regardless of the polarization state), only the $s_{0,\mathrm{out}}$ component of $\mathbf{S}_0$ can be measured. We obtained the value of $s_{0,\mathrm{out}}$ by multiplying the first row of the system Mueller matrix $\mathbf{M} = \mathbf{M}_{\mathrm{LP}}\mathbf{M}_{\mathrm{VR2}}\mathbf{M}_{\mathrm{VR1}}$ into the input Stokes vector $\mathbf{S}_i$:

$$
\begin{aligned}
s_{0,\mathrm{out}} = {} & s_0\left[\tfrac{1}{2}(q+r)\right] + s_1\left\{\tfrac{1}{2}(q-r)\left[\tfrac{1}{2}(1+\cos\delta)\cos\Delta\right.\right. \\
& \left.\left. - \frac{1}{\sqrt{2}}\sin\delta\sin\Delta\right]\right\} + s_2\left[\tfrac{1}{4}(q-r)(1-\cos\delta)\right] \\
& + s_3\left\{\tfrac{1}{2}(q-r)\left[\tfrac{1}{2}(1+\cos\delta)\sin\Delta\right.\right. \\
& \left.\left. + \frac{1}{\sqrt{2}}\sin\delta\sin\Delta\right]\right\}. \qquad (6)
\end{aligned}
$$

To recover the four components of the input Stokes vector, four measurements of $s_{0,\mathrm{out}}$ corresponding to four distinct sets of retardances Δ and δ are required. The resulting set of linear equations is solved by inversion, in matrix form $\mathbf{S}_i = \mathbf{A}^{-1}\mathbf{I}_0$, where the rows of $\mathbf{A}$ are the coefficients of s_0, s_1, s_2, and s_3 in Eq. (6) for each of the four pairs of retardance values (δ, Δ). For all the images presented in this paper, the retardance values were (δ, Δ) = (0°, 0°), (0°, 90°), (90°, 0°), and (90°, 90°).

4. Processing of Spectropolarimetric Images

To create a set of four polarization spectra at a particular horizontal location, we positioned the slit so that a vertical slice of the field was imaged, we used the VRFTSP to create an interferogram on the horizontal dimension of the FPA, and we made four independent polarimetric measurements at each location by varying the settings of the retarders. As discussed above, we obtained the second spatial dimension by scanning the target field. To maximize spatial and spectral resolution, the vertical extent of the slit and the image of the pupil in the horizontal direction should match the size of the FPA. For this experimental system, the spatial interferogram was slightly smaller than the FPA (typically $\sim 500 \times 300$ in a 640×480 image). This smaller size represented a trade-off between maximum resolution and storage space for the collected images.

Subtraction of dark current frames has been suggested to help remove bias caused by spatial variations in dark current across the FPA[12]; however, no such compensation was used with the VRFTSP. Fourier-transform spectrometers separate low-spatial-frequency noise that is due to dark current variations from the signal of interest in Fourier space. Subtracting a dark image from the acquired images is therefore unnecessary. In practice such a subtraction actually hurts the quality of the spectra. The deterministic, low-spatial-frequency information associated with the average dark current variation was eliminated because these average variations are highly correlated between images. The stochastic, high-spatial-frequency noise was not eliminated. In fact, the noise variance doubles in the subtracted spectra at high spatial frequencies because of the low degree of correlation in high-spatial-frequency noise from frame to frame (data not shown).

To minimize the effect of truncating the interferograms to the right and left edges of the image, we used a Hamming window. Use of a tapered window, such as the Hamming, Hanning, or raised cosine, is vital to reduce ringing (Gibbs phenomenon) in the Fourier-transformed spectra. The choice of window has an effect on the ability to discriminate two sources closely spaced in wavelength, but for the proposed application of the VRFTSP, image spectra are expected to vary smoothly. In this study, any smoothly tapered window produced nominally identical final spectral. No window is needed or desired in the vertical (imaging) dimension.

For the purposes of this paper, we used a coarse scan interval of 1 mm (in a field of ~25-mm width), but this did not seriously affect the images of the canonical targets described below. The coarse scan distance was used because of the serial nature of the processing as currently implemented. First, the four polarimetric images were obtained manually at each position, then the data were processed and the useful portions saved. Because of the manual operation, there was a practical limit of ~20 scan positions per image. If the process were automated, the scanning would be much more rapid.

After the polarimetric images were obtained at each scan location, they were saved to disk for further processing with MATLAB version 5.3. The images were imported into MATLAB, and we converted the spatial interferograms into spatiospectra by taking the Fourier transform of the windowed interferogram at each vertical position. A representative interferogram and the corresponding spectrum are presented in Fig. 2. As can be seen from Figs. 2(b) and 2(c), the interferograms at each spatial location were not symmetric because of placement of the image on the FPA and ghosting in the VRFTSP. For this reason, the absolute value of the Fourier transform is presented in Fig. 2(d). We calibrated the spectral axis by creating an interferogram of light transmitted through a narrow-band interference filter (10-nm FWHM centered at 600 and 650 nm). The calibration process is depicted in Fig. 3. The spectral sampling interval varied from target to target (because of changes in the amount of angular shear used in the interferometer) but was ~225 cm^{-1} (equivalent to ~8 nm at a wavelength of 600 nm).

Once the spatiospectral images were formed, the Stokes component images were computed as described in Section 3. The interferograms were not symmetric because of the optical setup, and the signal-to-noise ratio (SNR) was not as high as would be preferred, leading to a computed spectrum that is not necessarily real and positive. Therefore it was

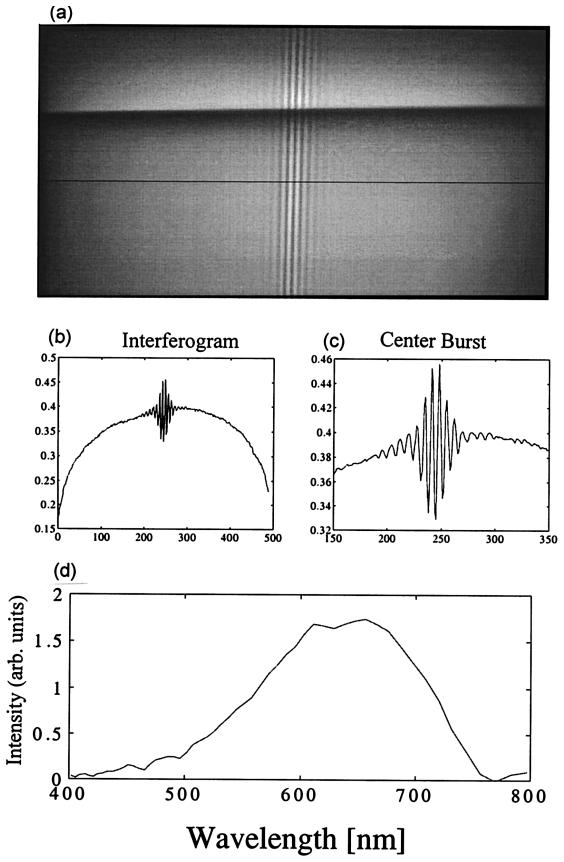

Fig. 2. (a) Representative spatiospectral image obtained with the slit at the center scan location (clear plastic) in Fig. 4(a). The optical system creates an interferogram in the horizontal direction and an image in the vertical, so each row in the image gives the interferogram at that vertical position within the slit. (b) and (c) The value of the interferogram along the black line in (a). (d) Absolute value of the Fourier transform.

essential to take the absolute value of the spectra before we formed the Stokes component images. To boost the SNR, we effectively converted the 8-bit digital-to-analog converter on the image processing board to a 13- or 14-bit digital to analog by adding 32 or 64 images at each location, thereby reducing the quantization noise. An additional factor that lowered the SNR was the imperfect beam splitter that limited the dynamic range of the device to 5 bits (which we effectively raised to 10 or 11 bits by adding images).

The result of the Mueller calculus was a set of four Stokes spatiospectral images corresponding to each horizontal location of the slit. We obtained the final spatial images at each spectral sample by rearranging the data so that the two dimensions of the image corresponded to the two spatial dimensions.

5. Experimental Images

To test the performance of the instrument, we imaged a series of canonical targets that exercised the capability of the VRFTSP to measure simultaneous variations in both the spectral content and the polarization state within an image. The first target

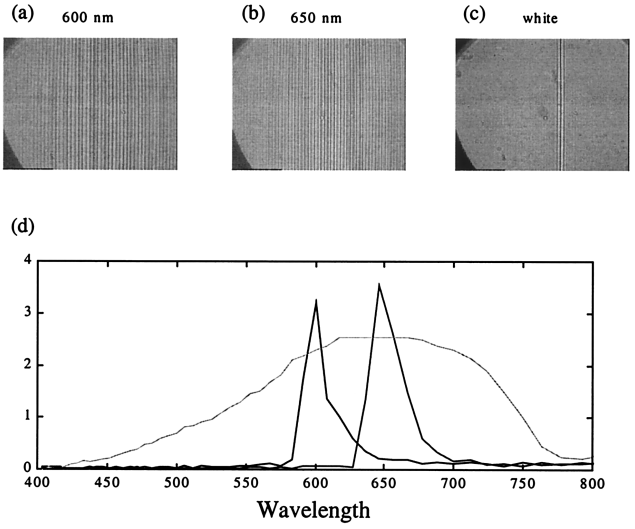

Fig. 3. Wavelength calibration process for the VRFTSP. We calibrated the spectral dimension by removing the cylinder lens L2 in Fig. 1 and allowing the interferogram to take up the entire FPA. (a) and (b) Interferograms obtained by use of 10-nm FWHM interference filters. (c) The white-light spectrum had no filter. (d) The average spectrum for each image.

was composed of a stack of plastic cylinder sections. Each cylinder was dyed a different color (one was clear, one was red, and one was blue), but they were the same size and shape. The stacked cylinders were positioned so that their axes were perpendicular to the direction of the slit used in the imager. A schematic of the target is shown in Fig. 4(a).

The diameter of the stack of cylinders was larger than the slit opening, so the slit was situated to image the top edge of the stack. The dotted area in Fig. 4 corresponds to the area imaged. The second and third canonical objects were 25.4-mm-diameter glass marbles. One marble was clear and the other was dyed green. Again, the marble diameter was larger than the slit, so the images did not include the entire object. A schematic of the setup for the marble targets is shown in Fig. 4(b).

The canonical targets that we chose make good test

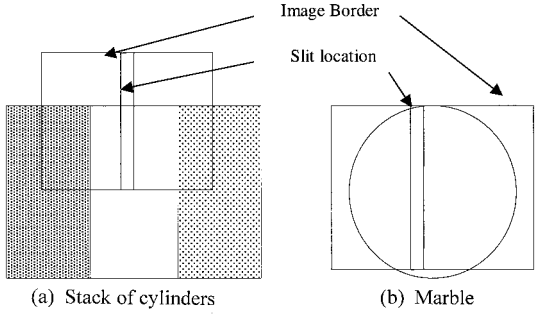

Fig. 4. Schematic of the target configurations. The dotted area corresponds to the portion of the scene that is imaged. The solid rectangle indicates the projection of the slit onto the target. The three plastics composing the stack of cylinders were dyed red, clear, and blue from left to right.

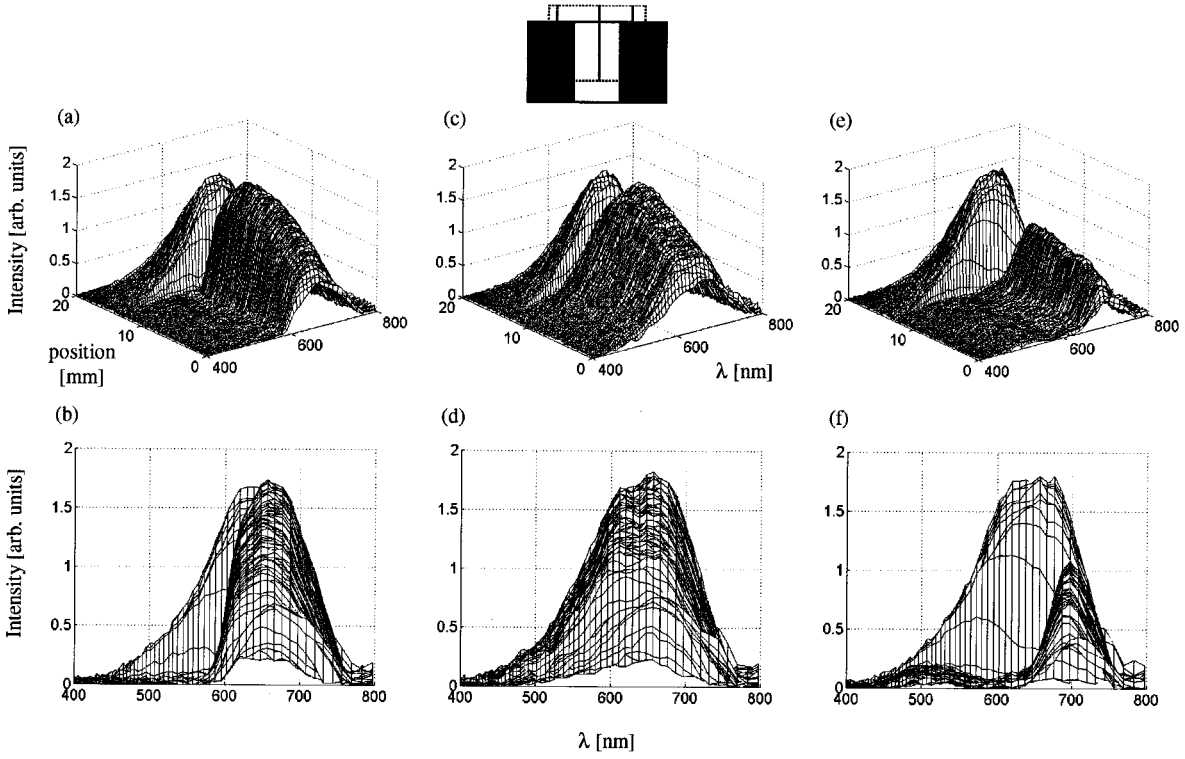

Fig. 5. Spatiospectral images of reconstructed s_0 at three horizontal scan locations on the stack of cylinders. The data correspond to the vertical lines on the inset: (a), (b) red plastic (leftmost location); (c), (d) clear (center location); (e), (f) blue (rightmost location). The bottom row of images is a two-dimensional projection of the three-dimensional data presented in the top row.

cases because of the predictable nature of the spatial variation of the polarization signal. To first order, the light that passes through the cylinder stack is expected to be partially vertically (p) polarized because of Fresnel reflection at the entrance and exit locations; the horizontally polarized component (s polarization) is preferentially reflected away at the entrance location, and the vertically polarized component is preferentially transmitted at the exit location. The light is expected to have a lower degree of polarization in the center of the cylinder as the incidence and exit directions approach normal. In addition, there may be a small region of specular reflection at the edge of the stack where the light is incident from a grazing angle.[5] The segmented nature of the stack results in a simple spatial variation of spectral content, as the transmitted spectra of the clear, red, and blue portions are expected to be different.

Similarly, the spheres provide targets with a constantly varying angle and degree of polarization, and the two nearly identically shaped objects with different apparent colors provide a test of the spectral capabilities of the VRFTSP. The expected angle of polarization of light transmitted at each position on the sphere is parallel to the projection of the local surface normal on the image plane.[5,13] There could also be a small specular band outside the edge of the marble.

A. Stack of Cylinders

The stack of cylinders was imaged in the configuration indicated in Fig. 4(a), and representative spectral data are presented in Fig. 5, which is composed of spatiospectral scans along the lines indicated in Fig. 4(a). Figures 5(a), 5(c), and 5(e) present two-dimensional maps of intensity versus position in spatiospectral space, and Figs. 5(b), 5(d), and 5(f) present the same maps projected onto the spectral axis. As indicated by the scan locations in Fig. 4(a), the top of each scan corresponds to the unpolarized white light that emerges from the diffusing screen behind the target. Approximately 7.5 mm from the top of the scan, the edge of the projected image of the cylinder is visible as a dark notch, and then the intensity increases as the scan moves toward the center of the cylinder. In the spectral dimension, the background portion of the scan provides information about the spectral content of the source. The source spectral content begins at approximately 750 nm (because of a filtering process that eliminates near-IR light in the source) and has little spectral content below 450 nm. It must be noted that the intensity plots presented here are uncalibrated. No attempt was made to compensate for the reduced response of the CCD at short wavelengths. The absolute performance of the interferometer can be inferred by one taking the ratio of spectra above and below the dark notch in Figs.

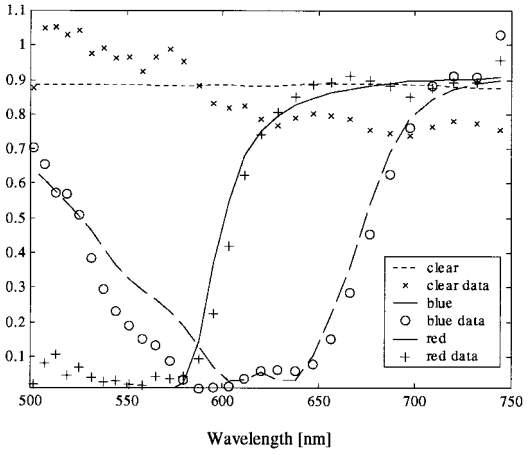

Fig. 6. Transmissivity data. We determined the transmissivity of the three plastics by taking the ratio between the 150th row and the 50th row at a single scan location for each color. The 50th row was well within the background, and the 150th row was well within the cylinder. The curves correspond to spectrophotometric measurements used for verification. Transmissivities greater than 100% result from the fact that data from different vertical positions within the image were used to infer the actual value. To account for the variations in thickness of the sample (because of curvature), a one-parameter least-squares fit was used to normalize the data obtained with the VRFTSP to match the curves from the spectrophotometer.

2(a) and 5 that marks the top of the target. Such ratios are presented in Fig. 6, along with independent transmissivity measurements made with a nonimaging spectrophotometer.

Figure 5 reveals interesting and unexpected information about the nature of the targets. To the human observer, the three plastics would be described as blue (scan position 1), clear (scan position 2), and red (scan position 3). However, Fig. 5 indicates that the transmissivity of the blue plastic in the near IR is no different from the transmissivity of the other two plastics. As expected, the blue plastic has high transmissivity at the short wavelengths, but one should be careful in inferring too much about relative intensity across the spectrum for the reasons discussed above. The clear plastic appears to have high transmissivity across the visible spectrum, whereas the red plastic acts as a long-pass filter and cuts off fairly sharply at ~600 nm. Note that this sharp cutoff is well represented by the spectrometer, and it is interesting to compare the nature of this spectral feature to the independent spectral measurements presented in Fig. 6.

To this point, only measurements of the unpolarized intensity s_0 have been presented. Scans of the other three Stokes parameters at position 2 are presented in Fig. 7. In Figs. 7(a), 7(c), and 7(e), the two-dimensional map of intensity versus position in spatiospectral space is presented, and in Figs. 7(b), 7(d), and 7(f), the projection of this map onto the spatial axis is presented. The wavelength range presented in Fig. 7 is reduced from that in Fig. 5 because of the sensitivity of the polarization measurements to SNR. Because the measured value of s_0 is used to normalize the other Stokes parameters, spurious results often result when the unpolarized intensity is small, as is evident near the edges of the maps in Fig. 7, as well as at the edge of the projected image of the cylinder where the intensity was low (see Fig. 5).

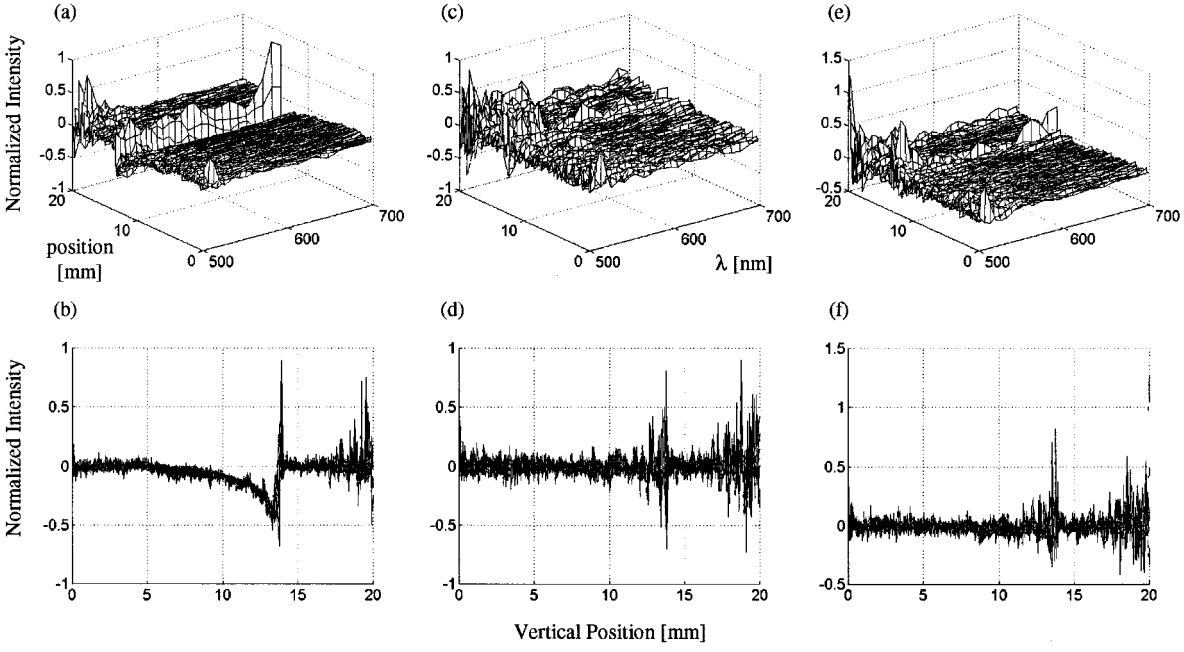

Fig. 7. Polarimetric data from the center section of the stack of cylinders. (a) and (b), s_1/s_0; (c) and (d), s_2/s_0; and (e) and (f), s_3/s_0. The data are presented between only 500 and 700 nm because the SNR is too low outside of this range. Note that the polarization signature of the target is wavelength independent, as should be expected.

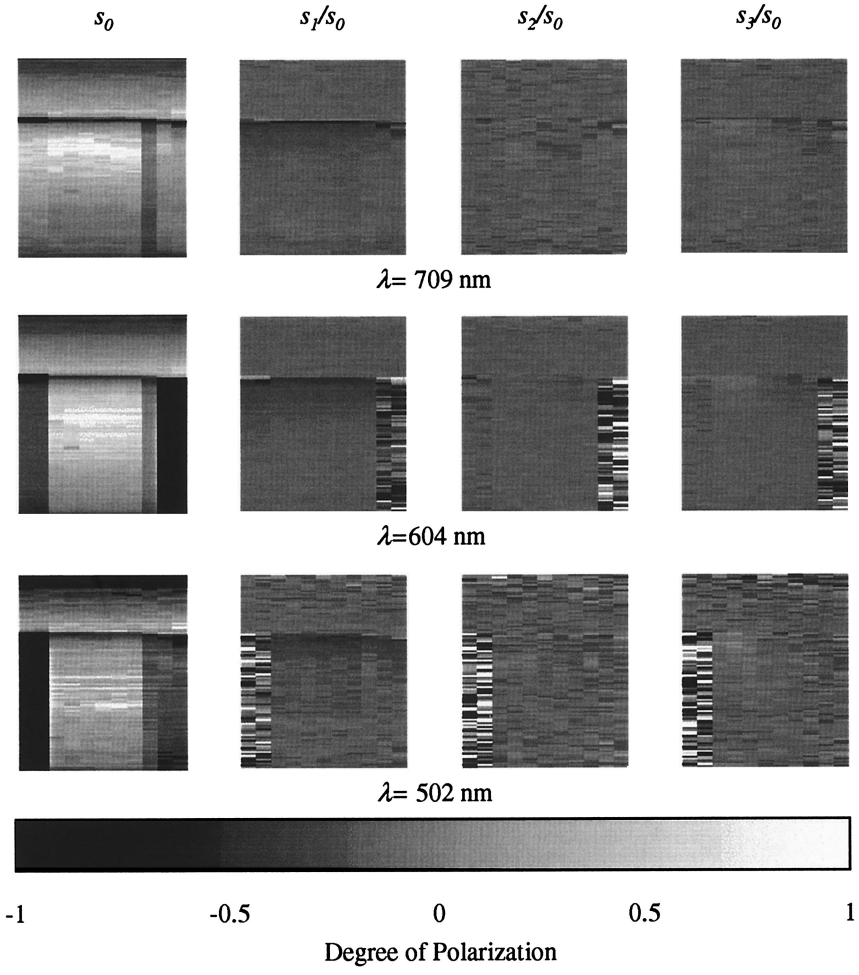

Fig. 8. Single-wavelength images of the stack of cylinders. Each row corresponds to the wavelength notations, and each column presents Stokes parameter images. All images are presented with the same gray scale. For s_1, light shades are partially horizontally polarized, and dark shades are partially vertically polarized. For s_2, light shades are 45° linearly polarized. For s_3, light shades are left-circularly polarized, whereas dark shades are right-circularly polarized. Noisy regions of the images correspond to areas with low values of s_0. These small values appear in the denominator of the normalized images.

Figure 7 presents polarimetric data that agree well with the predictions made above, as well as with previous measurements made on a similar target.[5] The light from the background appears unpolarized, there is a small highly horizontally polarized band of specularly reflected light just above the top edge of the cylinder, and a band of partially vertically polarized radiation transmitted through the cylinder that decays slowly in degree of polarization as the scan moves toward the center of the cylinder. There is less useful information in s_2 and s_3. However, there are definite trends in s_3 data that are discussed below and that agree with previously reported measurements.[5]

The reader should note that the scans of s_2 and s_3 appear to be noisier than the scan of s_1. This is an artifact of the specific Mueller calculus used for the processing. To distribute noise approximately equally in the Stokes images, the L_2 condition number of the inverse matrix used to compute the Stokes parameters from the intensity images should be minimized.[14,15] To accomplish this, one can run an optimization routine that would allow the angular and retardance settings to be manipulated to construct Stokes images with uniform noise in s_1, s_2, and s_3.[15]

The spatiospectral scans presented in Figs. 5 and 7 are one way to visualize the spatial distribution of the spectropolarimetric data. Another common way is the simultaneous presentation of two-dimensional polarimetric images at various distinct wavelengths.[1] Representative examples of such images for the stack of cylinders are presented in Fig. 8 corresponding to wavelengths of 709, 604, and 502 nm. These wavelength values were chosen to accentuate the differences in the transmitted spectra of the three cylinders (see Fig. 5). In each scan, the following images are presented from left to right: normalized s_0, s_1/s_0, s_2/s_0, and s_3/s_0. A comparison of the images from the different spectral bins shows that the differences in the transmissivity among the three plastics are evident. The distribution of vertically and horizontally polarized radiation is as described above. Except for the magnitude of the SNR, the polarimetric data (except for maybe s_3) do not differ

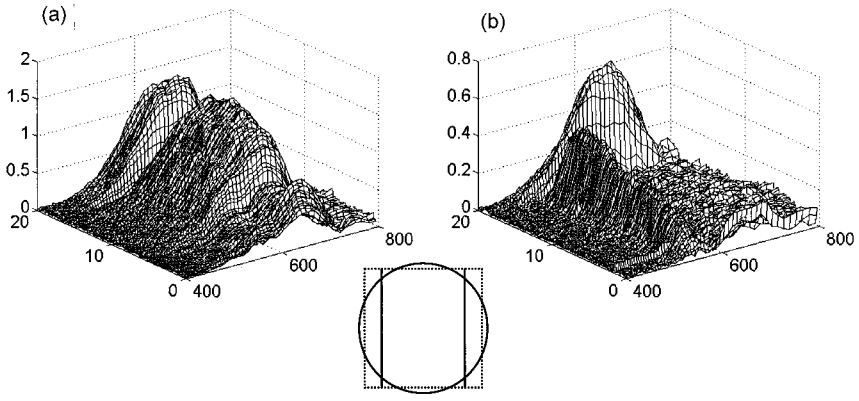

Fig. 9. Spatiospectral scans of s_0 on (a) the clear marble and (b) the green marble. The clear data are from the right scan line indicated on the insert, and the green data are from the left scan line. The decrease in intensity at approximately 3 mm in (a) is due to an inclusion in the glass marble.

in the three sections. Furthermore, the data have the same qualitative form in all spectral bins. Examination of the s_3 data reveals a trend that is evident in the clear portion of the stack and has been reported previously.[5] There appears to be a consistent partial circularly polarized contribution near the interfaces: partially left-circularly polarized at the left edge and partially right-circularly polarized at the right edge. It is not yet clear if this effect is real (possibly because of a total internal reflection interaction with the interface), and further investigation of this phenomenon is merited. Note that, although the boundaries between the three cylinders in the stack are clearly discernible through investigation of the s_0 spectral images, the boundaries are much less apparent in the other three Stokes parameter images (except, of course, where the SNR is so low that the image is completely noisy). This feature of the images clearly demonstrates the capability of the VR-FTSP to characterize spatially independent spectral and polarimetric information.

B. Spherical Targets

The two spherical targets described above were each imaged in the configuration depicted in Fig. 4(b). Spectral intensity data from a scan along position 1 in Fig. 4(b) on the clear sphere are presented in Fig. 9(a) and data from a scan along position 2 in Fig. 4(b) on the green sphere are presented in Fig. 9(b). Polarimetric images at 530 nm are presented in Fig. 10. There are several inclusions visible in the s_0 images of the clear sphere that are stable with respect to position across spectral bands that are not apparent in the polarimetric images. Similarly, the curvature features that are present in the polarimetric images are not evident in the normalized s_0 image. A two-dimensional polarization image formed by the mapping angle and the degree of linear polarization into the colorimetric parameters of hue and saturation is presented in Fig. 11 (Refs. 13, 16) for the clear marble in one spectral bin ($\lambda = 650$ nm).

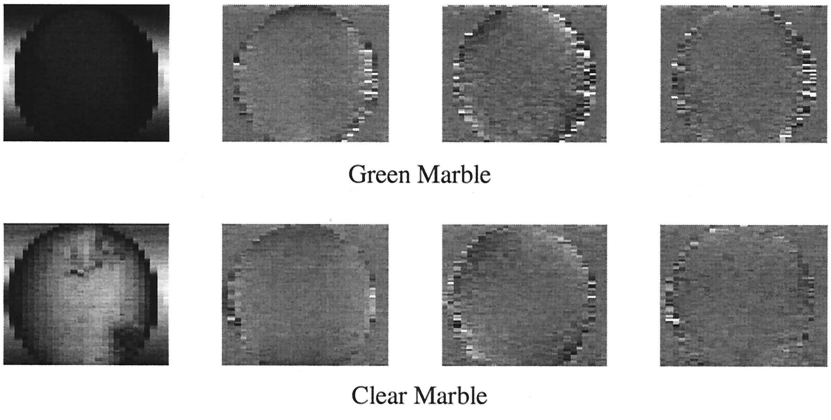

Fig. 10. Single-wavelength polarimetric images of the green and clear marbles. The data are from $\lambda = 530$ nm. From left to right the images are normalized s_0, s_1/s_0, s_2/s_0, and s_3/s_0.

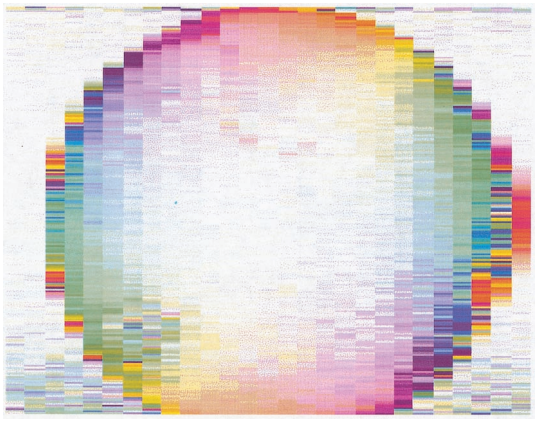

Fig. 11. Three-dimensional polarimetric image depicting the angle of linear polarization and the degree of linear polarization by use of the colorimetric parameters of hue and saturation, respectively. The color red corresponds to vertical polarization and cyan blue corresponds to horizontal. Highly saturated colors appear where the degree of polarization is high. These data are from the single-wavelength images at $\lambda = 650$ nm.

6. Conclusions and Future Research

The images presented here demonstrate the capability of the VRFTSP to compose fully seven-dimensional spectropolarimetric images of target scenes in a laboratory environment in the visible portion of the spectrum. Currently the major limiting factor of the device is the speed of processing. All imaging operations are currently performed serially, making the process of building up the spectropolarimetric scene time-consuming. The first necessary improvement is to automate the collection and scanning procedure, which will allow the VRFTSP to be developed into a brassboard unit capable of use in the field. However, for any real-time imaging applications, the collection strategy of the VRFTSP must be converted from serial to parallel to allow for imaging of targets that move relative to the platform.

A second factor limiting the performance of the VRFTSP is the SNR. New interferometer designs are being considered that will increase the dynamic range of the interferograms on the CCD and reduce the effect of ghosting at the image plane. In addition, use of parallel CCD's could allow for an overall increase in throughput by taking advantage of light that is currently discarded by either the interferometer or the input polarizer. As discussed above, optimization can be performed to distribute the noise more uniformly across the polarimetric parameters, thereby making s_1, s_2, and s_3 images more comparable.[13] Finally, although the research presented in this paper has been collected exclusively in the visible, the fundamental design of the device can be altered to allow development of a VRFTSP in the infrared.

References

1. L. J. Cheng, J. C. Mahoney, and G. Reyes, "Target detection using an AOTF hyperspectral imager," in *Optical Pattern Recognition V*, D. P. Casasent and T.-H. Chao, eds., Proc. SPIE **2237,** 251–259 (1994).
2. J. S. Tyo, M. P. Rowe, E. N. Pugh, Jr., and N. Engheta, "Target detection in optically scattering media by polarization-difference imaging," Appl. Opt. **35,** 1855–1870 (1996).
3. M. P. Silverman and W. Strange, "Object delineation within turbid media by backscattering of phase-modulated light," Opt. Commun. **144,** 7–11 (1997).
4. P.-Y. Gerligand, R. A. Chipman, E. A. Sornsin, and M. H. Smith, "Polarization signatures of spherical and conical targets measured by Mueller matrix imaging polarimetry," in *Polarization Measurement, Analysis, and Remote Sensing*, D. H. Goldstein and R. A. Chipman, eds., Proc. SPIE **3121,** 63–73 (1997).
5. T. S. Turner, Jr., and M. R. Hawks, "Ruggedized portable Fourier transform spectrometer for hyperspectral imaging applications," in *Remote Sensing for Agriculture, Forestry, and Natural Resources*, E. T. Engman, G. Guyot, and M. Marino, eds., Proc. SPIE **2585,** 222–232 (1995).
6. T. S. Turner, K. W. Peters, and J. S. Tyo, "Portable visible imaging spectro-polarimeter for remote sensing applications," in *Sensors, Systems, and Next-Generation Satellites II*, H. Fujisada, ed., Proc. SPIE **3498,** 223–230 (1998).
7. J. S. Tyo and T. S. Turner, Jr., "Imaging spectropolarimeters for use in visible and infrared remote sensing," in *Imaging Spectrometry V*, M. Descour and S. Shen, eds., Proc. SPIE **3753,** 214–225 (1999).
8. T. H. Barnes, "Photodiode array Fourier transform spectrometer with improved dynamic range," Appl. Opt. **24,** 3702–3706 (1985).
9. G. Vane, R. O. Green, T. G. Chrien, H. T. Enmark, E. G. Hansen, and W. M. Porter, "The airborne visible/infrared imaging spectrometer (AVIRIS)," Remote Sens. Environ. **44,** 127–143 (1993).
10. L. J. Rickard, R. Basedow, E. Zalewske, P. R. Silvergate, and M. Landers, "HYDICE: an airborne system for hyperspectral imaging," in *Imaging Spectrometry for Terrestrial Environments*, G. Vane, ed., Proc. SPIE **1937,** 173–179 (1993).
11. See, for example, R. Chipman, "Polarimetry," in *Handbook of Optics*, 2nd ed., M. Bass, ed. (McGraw-Hill, New York, 1996), Vol. 2, pp. 22.10–22.12.
12. L. J. Otten, III, A. D. Meigs, A. Franklin, R. D. Sears, M. W. Robinson, J. B. Rafert, D. S. Fronterhouse, and R. Grotbeck, "On board spectral imager data processor," in *Imaging Spectrometry V*, M. R. Descour and S. S. Shen, eds., Proc. SPIE **3753,** 86–94 (1999).
13. J. S. Tyo, E. N. Pugh, Jr., and N. Engheta, "Colorimetric representations for use with polarization-difference imaging of objects in scattering media," J. Opt. Soc. Am. A **15,** 367–374 (1998).
14. D. S. Sabatke, M. R. Descour, E. Dereniak, W. C. Sweatt, S. A. Kemme, and G. S. Phipps, "Optimization of retardance for a complete Stokes polarimeter," Opt. Lett. **25,** 802–804 (2000).
15. J. S. Tyo, "Noise equalization in Stokes parameter images obtained by use of variable retardance-polarimeters," Opt. Lett. **25,** 1198–1200 (2000).
16. G. D. Bernard and R. Wehner, "Functional similarities between polarization and color vision," Vision Res. **17,** 1019–1028 (1977).